Chapter 2
The ATLAS Experiment at LHC

This chapter introduces the main aspects of the ATLAS detector at the LHC collider. The reconstruction procedures of the physics objects that are relevant for the analyses described in this thesis (jets, electrons, muons and missing energy) are also discussed. The Appendix A describes dedicated studies carried out during the commissioning of the Tile hadronic calorimeter (TileCal), while Appendix B details the measurement of the instantaneous luminosity using the TileCal data.

2.1 Large Hadron Collider

The Large Hadron Collider (LHC) [1] is a particle accelerator designed to collide protons at a center of mass energy $\sqrt{s} = 14$ TeV. On the accelerator ring ($\sim$27 km in circumference) four detectors (ALICE [2], ATLAS [3], CMS [4] and LHCb [5]) have been built around the four interaction points to reconstruct and study the collisions delivered by the LHC.

Since 2010, the LHC has delivered proton-proton (p-p) collisions at center of mass energies of 7 and 8 TeV, about half of its nominal energy. The LHC has produced also lead ions (Pb-Pb) collisions with a per-nucleon center of mass energy $\sqrt{s_{NN}} = 2.76$ TeV and proton-ion (p-Pb) collisions with $\sqrt{s_{NN}} = 5.02$ TeV. More details about the delivered luminosity will be given below.

2.2 The ATLAS Detector

ATLAS (A Toroidal LHC ApparatuS) [3] is a general purpose detector designed for the reconstruction and identification of jets, photons, electrons, muons, taus and missing transverse energy. The detector has been designed to optimize the search for the Higgs boson and for a large number of searches for new phenomena.

V. Rossetti, *Search for Exotic Mono-jet Events*, Springer Theses,
DOI 10.1007/978-3-319-22225-7_2

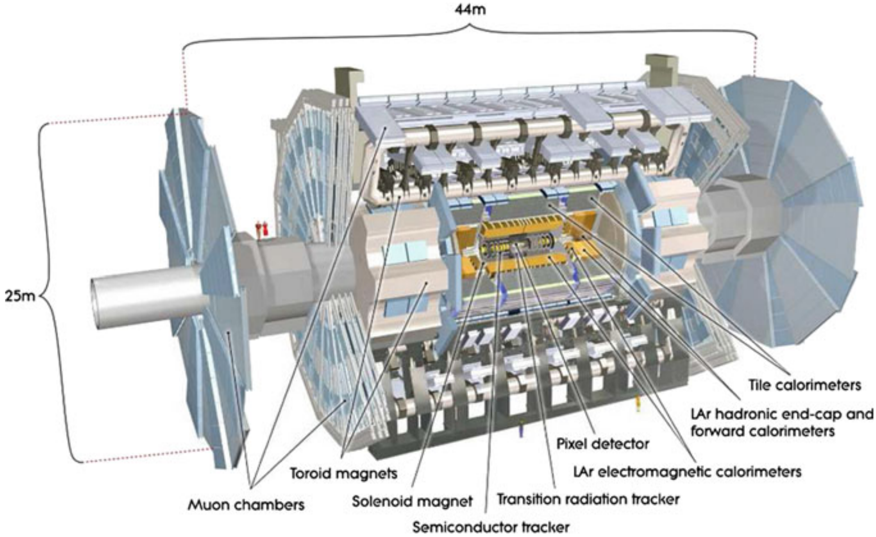

Fig. 2.1 Schematic view of the ATLAS detector

In the following, we will use a Cartesian right-handed coordinate system, with the origin in the nominal point of interaction, x axis pointing to the center of the LHC ring, and the y axis pointing upward. To define the direction of particles the following quantities are considered: the azimuthal angle $\phi = \arctan(y/x)$, and the pseudo-rapidity $\eta = -\ln(\tan(\theta/2))$, where θ is the polar angle defined from the z axis.

ATLAS is composed of different sub-detectors that we can divide in three different groups as treated in the following sections: the Inner Detector, the Calorimeters, and the Muon Spectrometer. A solenoidal magnetid field is used to bend the trajectories of the particles passing in the Inner Detector, while a toroidal magnetic field is used for the Muon Spectrometer. A sketch of the detector is presented in Fig. 2.1.

2.2.1 Inner Detector

The Inner Detector (ID) is the most inner part of ATLAS and occupies a cilindical volume around the LHC beam pipe. The ID has a radius of about 1.1 m and a length of 6.2 m along the beam pipe (see Fig. 2.2).

The ID has been designed to measure the properties of the charged particles generated in the collisions. Due to the high density of particles, a high granularity, a fast response and a good radiation resistence are needed to succesfully operated in the LHC environment. The ID is composed of three cylindrical concentric sub-detectors:

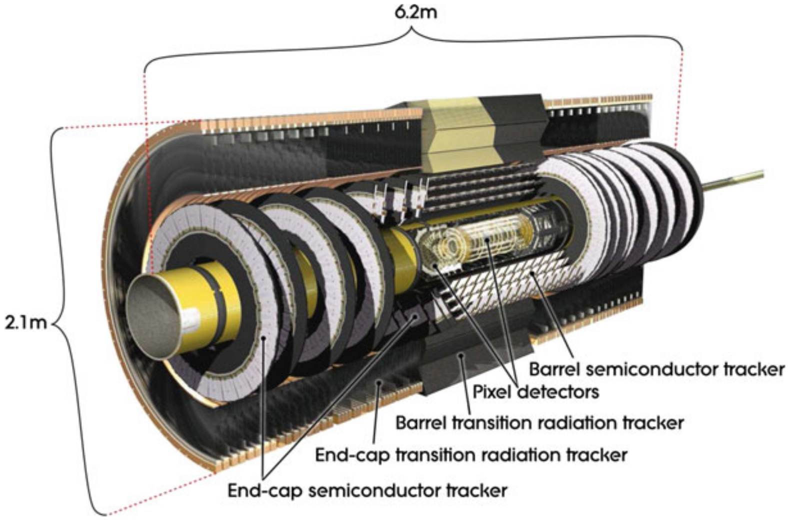

Fig. 2.2 Schematical view of the inner detector

- The Pixel detector measures charged particles using silicon sensors (pixels) and is the most inner part of the ID. The pixel sensors have a minimum size of 50 $\times$ 400 μm^2, and provide a resolution of 10 μm in the R-ϕ plane. Due to its high granularity, the Pixel detector has 80.4 milions read-out channels. This part of the ID mainly contributes to the precision vertex reconstruction.
- The Semiconductor Tracker (SCT) is a silicon microstrip detector, and is the middle part of the ID. This subdetector is composed of layers of stereo strips, so that approximately eight strips are crossed by each track and, since the position is determined from hits in overlapping strips, four space-points per track are usually available. Its sensors provide a resolution of 17 μm in the R-ϕ plane, and make use of 6.2 milions read-out channels. This sub-detector contributes mainly to the momentum reconstruction.
- The Transition Radiation Tracker (TRT) consists of 4 mm diameter gaseous straw tubes interleaved with transition radiation material, and enables tracking for $|\ \eta\ | < 2.0$. It only provides R-ϕ information, for which it has an accuracy of 130 μm per straw. The TRT is the most outern part of the ID and it has 351.000 readout channels. The TRT ease the track pattern recognition with its very large number of close hits (about 35 per track) and contributes to electron identification.

The first two are segmented in both r-ϕ and z, while the TRT is segmented only in r-ϕ. Using the combined information from the three subdetectors the transverse momentum resolution measured with cosmic muons [6] is:

$$\frac{\sigma_{p_T}}{p_T} = P_1 \oplus P_2 \times p_T, \tag{2.1}$$

where $P_1 = 1.6 \pm 0.1\,\%$ and $P_2 = (53 \pm 2)10^{-5}\,\text{GeV}^{-1}$. This translates in a resolution of 1.6 % for tracks with $p_\text{T} \sim 1\,\text{GeV}$ and of about 50 % for $p_\text{T} \sim 1\,\text{TeV}$.

2.2.2 Calorimeters

The ATLAS Calorimeter surrounds the ID and covers up to $|\eta| < 4.9$. It makes use of a lead and plastic tiles sampling calorimeter (TileCal) for the hadronic central part (up to $|\eta| < 1.7$) and a liquid Argon (LAr) calorimeter for the rest (see Fig. 2.3).

In total the calorimeter systems has 187,648 cells, and roughly 375,000 read-out channels. The cell granularity in ϕ and η varies between 0.025 in the electromagnetic (EM) central part, to 0.1 for most of the hadronic (HAD) sections, up to 0.4 for the most forward part of the hadronic calorimeter ($3.2 < |\eta| < 4.9$). The cells are organized in different layers in depth. The number of layers varies between three for the EM and the HAD central parts, to one for the EM section of the most forward part.

In the LAr calorimeter the liquid argon is the active medium, while the absorbers are either lead (for $|\eta| < 1.4$), or tungsten (for $1.4 < |\eta| < 4.9$ in the hadronic part), or copper for the rest. The liquid argon is kept at a temperature of 88 K with a cryogenic system, whose major components are housed between the LAr and the Tile calorimeters. Figure 2.4 (left) shows a sketch of the structure of one slice of the EM LAr calorimeter. Charged particles passing in the active material create couples of ions and electrons that drift in opposite directions by the presence of an electric

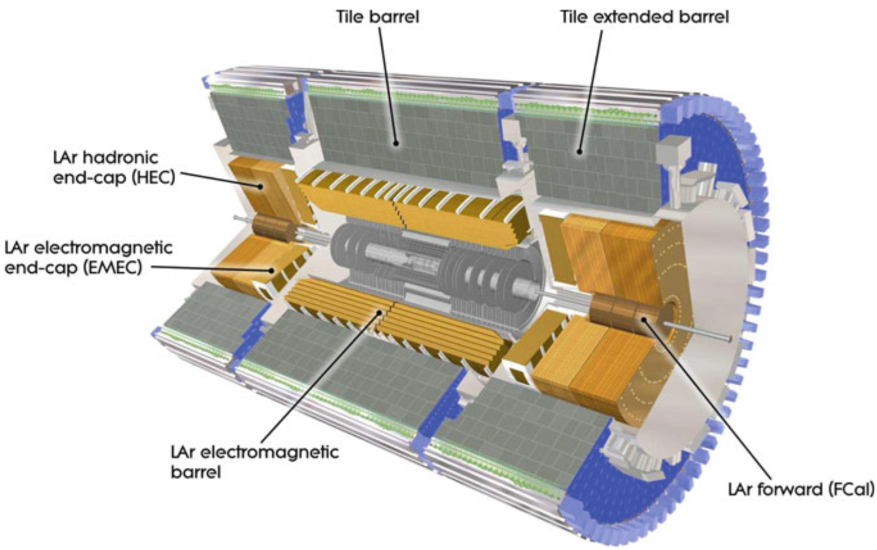

Fig. 2.3 Schematic view of the ATLAS calorimeters

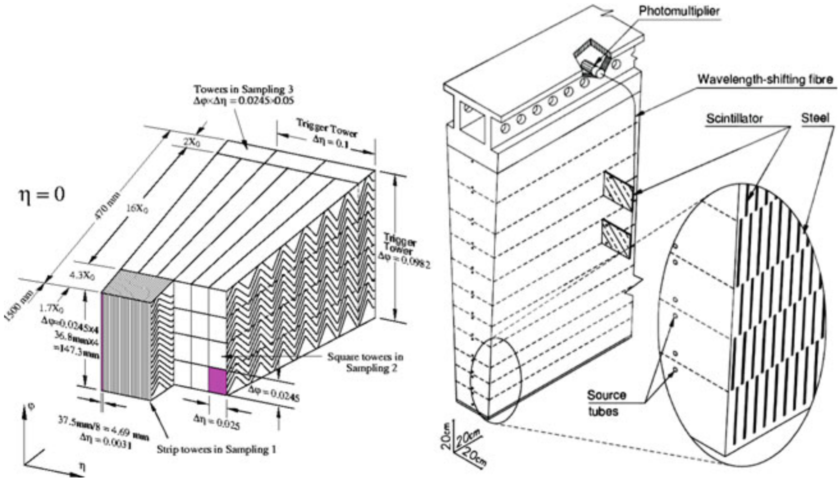

Fig. 2.4 Sketch of the structure of a LAr module (*left*) and a TileCal one (*right*)

field, and are collected by kapton electrodes. Different shapes of the kapton electrode surface have been used in order to provide a continuous calorimeter coverage in ϕ. For this reason an "accordion" geometry has been used for the central EM section (see Fig. 2.4 left), flat radial plates in the region $1.4 < |\eta| < 3.2$ both for the EM and HAD calorimeter, and tubes along the direction of the beam pipe for the most forward part. The relative energy resolution of the EM LAr calorimeter [7] is parametrized by:

$$\frac{\sigma_E}{E} = \frac{10\,\%}{\sqrt{E}} \oplus \frac{170\,\text{MeV}}{E} \oplus 0.7\,\% \tag{2.2}$$

TileCal is a sampling calorimeter with lead as absorbed and tiles of plastic scintillator as active material (see Fig. 2.4 right). The tiles emit light when charged particles pass through them. The light is collected by optical fibers and converted in pulses by photomultipliers. For TileCal the energy resolution is

$$\frac{\sigma_E}{E} = \frac{50\,\%}{\sqrt{E}} \oplus 3\,\%, \tag{2.3}$$

measured with test-beam data [8].

For both calorimeters the conversion factors between the reconstructed electronic signals and the deposited energy (called electromagnetic scale, or EM scale) have been determined by test-beam measurements with electrons in a range of 10–350 GeV. The electromagnetic scales have been validated with test-beam muons, cosmic muons, and E/p studies at collisions. Using collision data, the EM scale of the electromagnetic calorimeter has been corrected to reproduce the Z mass peak central value. The corrections are of the order of 1 %.

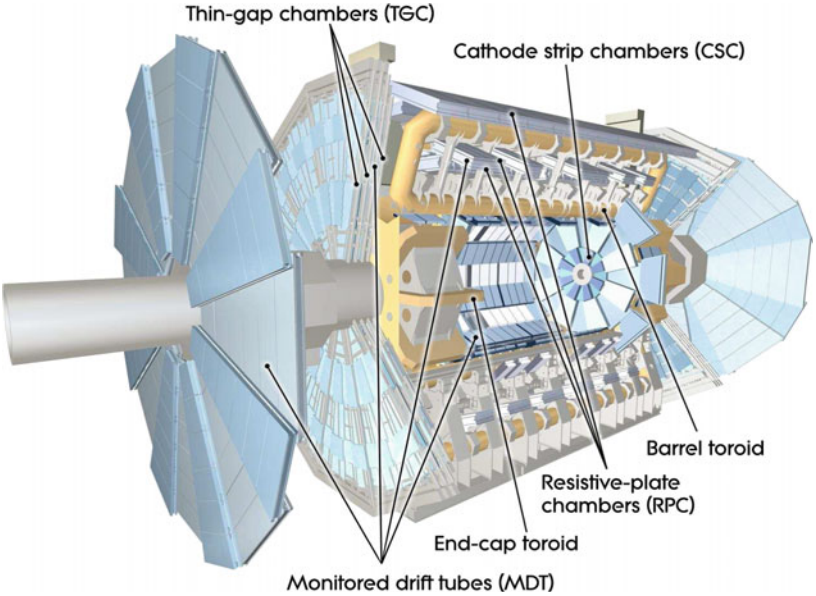

Fig. 2.5 Schematic view of the ATLAS muon spectrometer

The main aspects of the TileCal commissioning with cosmic muons, single beam data and first collision events are discussed in Appendix A.

2.2.3 Muon Spectrometer

The Muon Spectrometer is the most outer part of the the ATLAS detector and has been designed to identify and measure high momentum muons (see Fig. 2.5). The Muon Spectrometer is composed of four sub-detectors that make use of different technologies: Monitored Drift Tubes (MDT), Cathode Strip Chambers (CSC), Resistive Plate Chambers (RPC) and Thin Gap Chambers (TGC).

These sub-detectors are immersed in a magnetic field, generated by three toroids: one covers the central pseudo-rapidity range (approximately $|\eta| < 1.5$) providing a 0.5 T field, and other two, placed at higher pseudo-rapidity ($|\eta| > 1.5$), generating a 1 Tesla field. Each of them consists of eight coils assembled radially and symmetrically around the beam axis. The magnet configuration provides a field which bends the muon trajectories along the θ angle.

The MDT chambers perform a precision coordinate measurement in the bending direction of the air-core toroidal magnet, and therefore provide the muon momentum measurement for most of the eta range ($|\eta| < 2.7$). The basic detection element is a cylindrical aluminium drift tube of 3 cm diameter and a central wire at a potential of 3080 V. The drift tube is filled with a gas composed of Ar (93 %) and CO_2 (7 %). Muons passing in the tubes produce ionization charges that are collected on the wire. The reconstructed drift time provides a precise measurement of the minimum distance between the muon and the wire (with a typical resolution of 80 μm), and it's used to reconstruct the muon trajectory.

The CSC are multi-wire proportional chambers with cathodes segmented into strips, and are used at large pseudo-rapidities ($2.0 < |\eta| < 2.7$) in order to cope with the higher muon rate and background conditions. RPC and TGC are used for the trigger (see below) and measure also the muon ϕ coordinate.

2.2.4 Trigger System

In the last years, the LHC has been operating with a minimum time spacing of 50 ns between two bunch crossings. This translates into a maximum input rate of events of 20 MHz. The ATLAS trigger system is designed to bring this rate to 100 Hz, in order to record and store permanently the event information. The trigger system is organized in three levels: level 1 (LVL1), level 2 (LVL2), and Event Filter (EF). Each level refines the decision made at the previous step and, if necessary, applies additional selection criteria.

The LVL1 selects events with large missing energy or for high momentum muons, electrons, photons, tau and jets. The time available for the decision is 2.5 μs at most, therefore a simplified reconstruction of the physics objects is implemented. The LVL1 brings the rate of events to approximately 75 kHz.

The LVL2 has access to nearly all sub-detector information in a specific $\eta \times \phi$ region (called Region of Interest) around the objects selected at LVL1. The average event processing is 40 ms. The LVL2 brings the rate of events down to approximately 1 kHz.

The EF uses refined reconstruction algorithms that are very close to those used offline. The available time for event processing is 4 s in average, and the rate of events is reduced to approximately 100 Hz.

2.2.5 Luminosity Measurement

A precise luminosity determination is an essential ingredient for all physics analysis. In ATLAS, the luminosity is determined with several sub-detectors, each of them using different techniques [9, 10].

The luminosity can be expressed as:

$$L = \frac{n_b f_r n_1 n_2}{2\pi \Sigma_x \Sigma_y}, \tag{2.4}$$

where n_b the number of proton bunches crossing at the interaction point, and f_r the frequency of the LHC machine, n_1 and n_2 are the number of protons in the two LHC beams, and Σ_x and Σ_y characterize the horizontal and vertical profiles of the beams. In order to measure directly Σ_x and Σ_y, the two LHC beams are moved in steps of known distance, on both the horizontal and vertical direction. This special operation is called "van der Meer scan", or vdM scan. The absolute luminosity can therefore be measured at a vdM scan using Eq. 2.4, and knowing the currents of both LHC beams.

In order to relate the luminosity and μ, the average number of interaction per bunch crossing, the luminosity can be written as:

$$L = \frac{R_{inel}}{\sigma_{inel}} = \frac{\mu n_b f_r}{\sigma_{inel}}, \tag{2.5}$$

where σ_{inel} is the total inelastic cross section, R_{inel} is the rate of inelastic collisions, that can be written as product of n_b, f_r, and μ.

The visible number of interactions is defined as $\mu_{vis} = \epsilon\mu$, where ϵ is the efficiency of a particular sub-detector and a given algorithm to determine μ. Equation 2.5 can be rewritten as:

$$L = \frac{\mu_{vis} n_b f_r}{\sigma_{vis}}, \tag{2.6}$$

where σ_{vis} is the visible inelastic cross section, that can be retrieved at the vdM scan combining Eqs. 2.4 and 2.6. Therefore the luminosity is determined for a given measure of μ_{vis} through Eq. 2.6.

In order to measure μ_{vis} with a sub-detector, ATLAS primarily uses event counting algorithms, for which the number of events that satisfy a given criteria (typically a number of hits above a certain threshold) is compared with the total number of bunch crossings.

The default luminosity measurement in ATLAS for the 2011 and 2012 datasets was made using the Beam Conditions Monitor (BCM) [11]. The BCM is a fast device primarily designed to monitor background levels and issue a beam-abort request in case beam losses start to risk damage to ATLAS detectors. BCM consists of four small diamond sensors on each side of the ATLAS interaction point arranged around the beampipe in a cross pattern. In order to measure μ_{vis} with BCM, different event counting algorithms are used. The simplest algorithm requires a hit in either one of the two BCM arms (either at positive or negative η), and is called BCM_OR. At the vdM scan $\mu_{vis} \ll 1$, so that the probability to select an event with this algorithm is

$$\frac{N^{OR}}{N^{TOT}} = 1 - e^{-\mu_{vis}^{OR}}, \tag{2.7}$$

where N^{OR} is the number of bunch crossings that fulfilled the BCM_OR requirement, and N^{TOT} is the total number of bunch crossings.

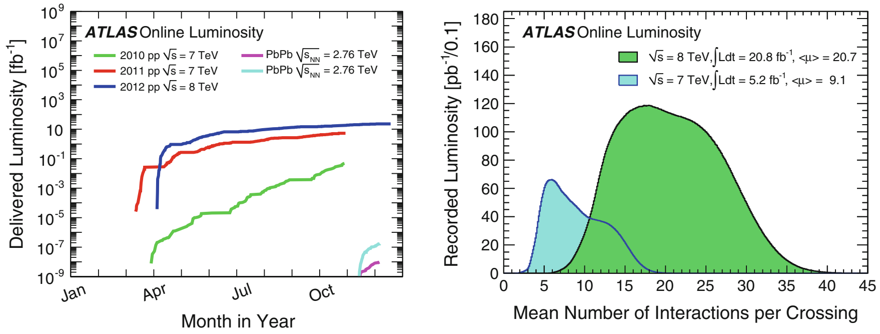

Fig. 2.6 Total integrated luminosity delivered by LHC in both p-p and Pb-Pb collisions from 2010 to 2012 (*left*). Mean number of interactions per bunch crossing in 2011 and 2012 p-p data (*right*)

For the p-p collisions realized until now the maximum instantaneous luminosity has been $7.7 \times 10^{33}\,\mathrm{cm}^{-2}\,\mathrm{s}^{-1}$, while for Pb-Pb and Pb-p collisions it has been 5.1×10^{26} and $1.1 \times 10^{29}\,\mathrm{cm}^{-2}\,\mathrm{s}^{-1}$ respectively. Figure 2.6 (left) shows the integrated luminosity of the various kinds of collision delivered from 2010 to 2012. Figure 2.6 (right) shows instead the μ distribution in the full 7 and 8 TeV datasets. Comparisons between the luminosity measured with BCM, TileCal and other sub-detectors are presented in Appendix B, which gives more details about the luminosity measurement using TileCal for both the 7 and 8 TeV data.

2.3 Reconstruction of Physics Object

This section describes the reconstruction of electrons, muons, jets, and missing transverse energy, giving emphasis to the aspects that are more important for the analyses presented in the next chapters.

2.3.1 Electrons

In the pseudo-rapidity region where the Inner Detector is operational ($|\eta| < 2.5$), electron candidates are defined by a matching between a track and a energy deposit in the EM calorimeter. The energy deposit is defined by a cluster of adjacent towers in $\eta \times \phi$. Each tower sums the energy in each cell in a region $\Delta\eta \times \Delta\phi = 0.025 \times 0.025$. The cluster of towers have size 3×7 in $\eta \times \phi$ for the calorimeter region $|\eta| < 1.4$, and 5×5 for the rest.

Tracks used for the electron candidates are reconstructed with an inside-out strategy. The track candidates built with the pixel detector and the first SCT layer are extrapolated to the outer part of the Inner Detector. Trajectories are fitted and fake tracks are rejected by applying quality cuts. Trajectories are extrapolated to the calorimeter and the track with smallest ΔR with respect to the calorimeter cluster is taken for the electron reconstruction.

To reject fake electrons, mainly from jets, quality requirements on calorimeter and tracking information have been defined [12]. For the analyses presented in this thesis, these requirements are:

- Small or no leakage of energy in the hadronic calorimeter,
- Narrow shape of the calorimeter shower consistent with real electrons,
- Associated track with more than 6 hits in the pixel and SCT layers, with at least one hit in the Pixel and a transverse impact parameter $d_0 < 5$ mm,
- Matching between track and calorimeter cluster with $\Delta\eta < 0.01$.

For the first two requirements the actual cuts depend on the electron energy and pseudo-rapidity [12].

The η, ϕ directions of the electron are taken from the associated track. For the 7 TeV analyses, the electron energy is taken from a weighted average between the track momentum and the cluster energy, while for 8 TeV analyses only the calorimeter information is used. The energy is corrected for dead material and for lateral and longitudinal leakage, with MC-based factors. These corrections have been validated in test-beams.

2.3.2 Muons

Muon candidates are reconstructed using Inner Detector and the Muon Spectrometer information [13]. The hits in each station of the Muon Spectrometer are combined to build track segments up to $|\eta| < 2.7$. For the analyses described in this thesis, muon candidates are reconstructed with two alternative procedures:

- "Combined" muon reconstruction. First, muon candidates are reconstructed using only Muon Spectrometer segments. The muon momentum measured in the Muon Spectrometer is corrected for the parametrized energy loss of the muon in the calorimeter, to obtain the muon momentum at the interaction point. Second, a match with a Inner Detector track is required and the momentum of the stand-alone muon is combined with the momentum measured in the Inner Detector.
- "Segment Tagged" muon reconstruction. A track in the inner detector is identified as a muon if the trajectory extrapolated to the Muon Spectrometer can be associated with straight track segments.

Combined muons are the highest purity muon candidates. Tagged muons give additional efficiency as they can recover muons which did not cross enough precision chambers to allow an independent momentum measurement in the Muon Spectrometer. Typical cases are low p_{T} muons ($p_{\mathrm{T}} < 20$ GeV) that only reach the inner layer of precision chambers or less instrumented detector regions. In order to reject fake muons, all associated Inner Detector tracks are required to pass quality criteria based on the number of hits in the pixel, SCT and TRT systems.

2.3.3 Jets

In the analyses presented in this thesis, jets are reconstructed using the anti-kt algorithm [14], with jet radius parameter R $= 0.4$. The constituents of the jet finding algorithm are calorimeter clusters of energy, also called "topo-clusters"[15], defined as follow.

Jet constituents Topo-clusters are built out of neighboring calorimeter cells with significant energy deposit over the noise. The noise is measured for each cell independently, and it is defined as the expected RMS of the electronic noise for the current gain and conditions plus the contribution from pileup added in quadrature. In order to make topo-clusters, all cells with a signal to noise ratio |S/N| ≥ 4 are taken as seed cells for a topo-cluster formation. These cells are considered in descending order of S/N, and all neighboring cells with |S/N| ≥ 2 are added to the topo-cluster. Subsequently all cells adjacent to a topo-cluster cell are added, independently of their S/N. Final topo-clusters are treated as massless and their energy, at the electromagnetic scale, is the sum of the energies of the cells belonging to the topo-cluster.

Jet finding algorithm The anti-kt algorithm is a sequential recombination algorithm and is used in ATLAS in order to define the jets. For all constituents the algorithm computes the following quantities:

$$d_{ij} = \min\left(\frac{1}{k_{ti}^2}, \frac{1}{k_{tj}^2}\right)\frac{\Delta R_{ij}^2}{R^2} \quad \text{and} \quad d_{iB} = \frac{1}{k_{ti}^2}, \tag{2.8}$$

where k_{ti} is the transverse momentum of constituent i, $R_{ij} = \sqrt{\Delta\eta^2 + \Delta\phi^2}$ between constituents i and j, and R a parameter of the algorithm that approximately controls the size of the jet. The distance d_{iB} is introduced in order to separate constituents coming from the hard interaction and those coming from proton remnants. The smallest distance is found, and if it is d_{ij}, constituents i and j are combined into one single object. If instead it is d_{iB}, constituent i is considered a jet and is removed from the list. The distances are recalculated with the remaining objects, and the process repeated until no constituent is left in the list. Once the process is finished, the jet four-momenta are defined by the vectorial sum of all the four-momenta of the topo-clusters belonging to it, so that the jet can have mass $m_{jet} > 0$. After this procedure, jets are defined with a minimum transverse momentum threshold p_{T}^{jet}, that is used as a scale to separate soft and hard physics.

Sequential recombination algorithms are very convenient because they are collinear and infrared safe to all orders in pQCD, as well as computationally fast. The anti-kt algorithm has been chosen because is particularly performant against pile-up, since it starts summing up constituents with higher momentum and produces jets with a conical structure.

Pile-up corrections Subsequently, corrections can be applied to subtract the energy contributions from multiple interactions from the same or previous bunch-crossings [16]. These corrections depend on the jet pseudo-rapidity and are parametrized as a function of the number of reconstructed vertex in the event, and on the average number of interactions μ.[1] The effect of pile-up on a central anti-kt jet with $R = 0.4$, is an over-estimation of the jet energy of about 0.2 GeV for each additional interaction in the same bunch-crossing. Multiple interactions in previous bunch-crossings, instead cause an under-estimation of the energy due to the particular LAr signal pulse shape. These two effects, therefore, tend to compensate. For the analysis of the 7 TeV data presented in this thesis, the effect of the pile-up corrections is very small and considered negligible; therefore these corrections are not applied. On the contrary, due to the higher pile-up level, corrections are applied in the analysis of the 8 TeV dataset.

Jet calibration The EM scale needs to be further calibrated to account for calorimeter non-compensation (the energy response to hadrons is lower than the response to electrons of the same energy), dead material (inactive regions of the detector where energy is lost) and leakage (energy deposits from particles which shower is not fully contained in the calorimeter). Moreover, corrections are needed for low momentum particles that are deflected by the magnetic field, and for energy losses in topo-cluster formation, and jet reconstruction. In order to correct for all these effects, a jet energy scale (JES) correction as a function of the jet energy and pseudo-rapidity is applied to jets at the EM scale [17]. The corrections are derived from di-jet MC samples produced with PYTHIA 6.423 with the AMBT1 tune. Calorimeter EM-scale jets are matched in ΔR with "truth" jets, that are reconstructed from stable particles in the final state,[2] excluding muons and neutrinos. Also the truth jets are built with the anti-kt algorithm with $R = 0.4$. The correction factors are based on the ratio of energies of the two matched jets E^{calo}/E^{truth}. It is important to mention that the calorimeter response in MC simulations has been extensively tested in both test beams and collision data. Figure 2.7 shows this ratio for different calibrated jet energies and as a function of the pseudo-rapidity of the reconstructed jet. The inverse of the response shown in each bin is equal to the average JES correction.

The reconstructed pseudo-rapidity direction can be biased due to the calorimeter response in different η regions. This effect is also corrected with MC-based correction factors. The η correction is about 0.01 for most of the calorimeter regions, and goes up to 0.05 in the transition regions between the different calorimeters. Jet four-momenta are also corrected to refer their kinematics to the primary vertex. This correction improves slightly ($\leq 1\,\%$) the jet p_T response.

[1] The μ is measured every minute, so that it gives information about the average number of interactions in neighboring bunch-crossings.

[2] The final state in the MC generators is defined using all particles with lifetime above 10^{-11} s.

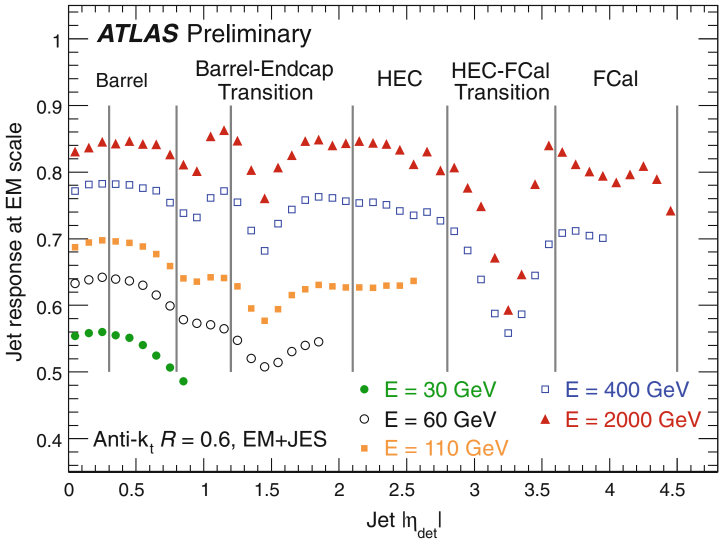

Fig. 2.7 Calorimeter response to jets before calibration in different pseudo-rapidity regions and for different energies. The inverse of the response shown in each bin is equal to the average jet energy scale correction

Jet energy scale uncertainty The jet energy scale (JES) uncertainty [18] comes mainly from the uncertainty on the single particle response, and has been estimated with E/p studies on isolated hadrons. Other leading uncertainties come from the limitations in the detector knowledge (such as the amount of dead material), and the physics models and parameters (mainly fragmentation and underlying event) in the MC event generator used to derive the JES corrections, the effects of having multiple interactions per bunch-crossing, and presence of close-by jets. Most of these uncertainties have been estimated for jets with $|\eta| < 0.8$ and then propagated to the more forward regions with the method of the p_T balance in di-jet events (see Ref. [19]). The reason is that the detector is better known in the central region, and that test-beam measurements to estimate the uncertainty due to the calorimeter response to single particles were only performed in the range $|\eta| < 0.8$.

For the 7 TeV data, the total JES uncertainty in absence of pile-up and near-by jets varies between 2.5 % for central high-p_T jets ($|\eta| < 0.8$, $60 < p_T < 800$ GeV) and 14 % for forward low-p_T jets ($3.2 < |\eta| < 4.5$, $20 < p_T < 30$ GeV). Close-by jets with $\Delta R < 0.7$ introduce an additional uncertainty of 2–3% dependently of the rapidity and the p_T of the jets. Multiple interactions in the same bunch-crossings introduce, for jets with $p_T = 30$ GeV ($p_T = 100$ GeV), an uncertainty of 0.5 % (0.1 %) for each reconstructed vertex. Figure 2.8 (left) shows the combination of all JES uncertainties for anti-kt jets with R = 0.6,[3] in $0.3 < |\eta| < 0.8$.

[3]Note that in this thesis jets are reconstructed with R = 0.4. JES uncertainties on jets with R = 0.4 and 0.6 are comparable.

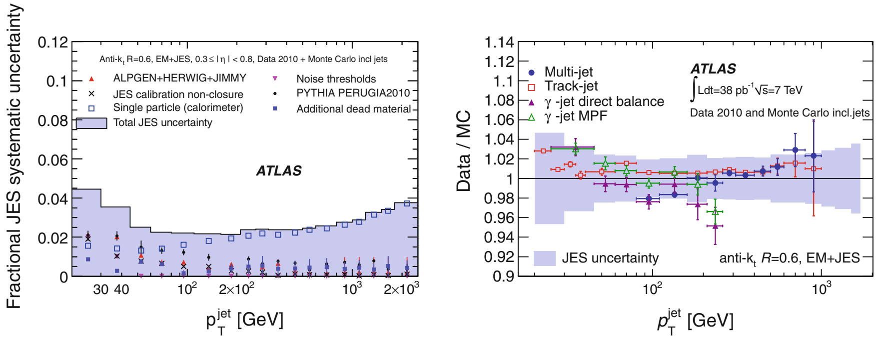

Fig. 2.8 The figure on the *left-hand side* shows the different contributions of the JES uncertainties for anti-kt jets with R = 0.6, in $0.3 < |\eta| < 0.8$, as a function of the jet p_T. The figure on the *right-hand side* shows the data-MC comparison on the jet response in various in-situ techniques, that is meant to validate the JES uncertainty

The JES is validated for jet p_T up to 1 TeV to the level of a few percent using several in situ techniques by comparing a well-known reference such as the recoiling photon p_T, the sum of the transverse momenta of tracks associated to the jet, or a system of low-p_T jets recoiling against a high-p_T jet. The JES systematic uncertainty determined from the combination of these in situ techniques are consistent with the one derived from single hadron response measurements over a wide kinematic range. Figure 2.8 (right) presents the ratio of data and MC jet responses in $|\eta| < 1.2$, compared with the JES uncertainty, showing compatible results.

Jet energy resolution The jet energy resolution (JER) [20] is measured with the in-situ techniques of the bisector [21] and the di-jet balance [22] methods, and the results are found in agreement within uncertainties. For jets with $p_T > 100$ GeV and $|\eta| < 0.8$ the JER is below 10 %, while is 15 % for jets with $p_T = 30$ GeV and $2.1 < |\eta| < 2.8$. Overall, the MC simulation of the JER agrees with the data within 10 %.

2.3.4 *Missing Transverse Energy*

In ATLAS there are different ways for calculating the missing transverse energy (E_T^{miss}). The most used method associates the calorimeter topo-clusters to reconstructed objects, such as jets, electrons, muons, taus, and photons, and calibrates them accordingly. In the next chapters we will use a E_T^{miss} made with a simpler calibration scheme, called "Local Cluster Weighting" (LCW) [23], that is more suitable for the analyses described in this thesis.

The LCW calibration method classifies the topo-clusters as either electromagnetic or hadronic, using the energy density and the shape of the cluster. Based on this classification energy corrections are derived from single pion MC simulations.

Dedicated corrections are derived for the effects of non-compensation, signal losses due to noise threshold effects, and energy lost in non-instrumented regions. They are applied to calorimeter clusters and are defined without reference to a given reconstructed object. They are therefore called local corrections. A special correction is made for the energy lost in the cryostat between the LAr electromagnetic calorimeter and the Tile calorimeter, which at a thickness of about half an interaction length can lead to signicant energy losses in hadronic showers.

After the topo-cluster four-momenta are calibrated the $E_{\mathrm{T}}^{\mathrm{miss}}$ is calculated form the vectorial sum of the p_{T} of all cells belonging to topo-clusters:

$$E_x^{\mathrm{miss}} = -\sum_{i=1}^{N_{cell}} E_i^{cell} \sin(\theta_i)\cos(\phi_i) \qquad E_y^{\mathrm{miss}} = -\sum_{i=1}^{N_{cell}} E_i^{cell} \sin(\theta_i)\sin(\phi_i) \tag{2.9}$$

The $E_{\mathrm{T}}^{\mathrm{miss}}$ performance can be studied by measuring the $E_{x,y}^{\mathrm{miss}}$ resolutions as function of the total transverse energy ΣE_T, which is reconstructed from the calorimeters as the scalar sum of the transverse energy of all cells. Figure 2.9 (left) shows the $E_{\mathrm{T}}^{\mathrm{miss}}$ resolution in minimum-bias events at 7 TeV. The $E_{\mathrm{T}}^{\mathrm{miss}}$ resolution is expressed as the root mean square of the $E_{x,y}^{\mathrm{miss}}$ distributions, and follows approximately a $k \times \sqrt{\Sigma E_T}$ function, with k being a parameter to be fitted. Three calibration schemes are compared in the figure: the LCW, the EM (topo-cluster four-momenta are used at the EM scale), and the "Global Cell Weighting", or GCW (see Ref. [24]). The latter applies cell-level weights that are based on the comparison between reconstructed and truth jets in MC. The figure shows how the LCW and GCW calibration schemes improve the $E_{\mathrm{T}}^{\mathrm{miss}}$ resolution. Figure 2.9 (right) compares instead the $E_{\mathrm{T}}^{\mathrm{miss}}$ resolution in data and MC events, showing a good agreement. For the simulation, samples of PYTHIA minimum-bias events have been used.

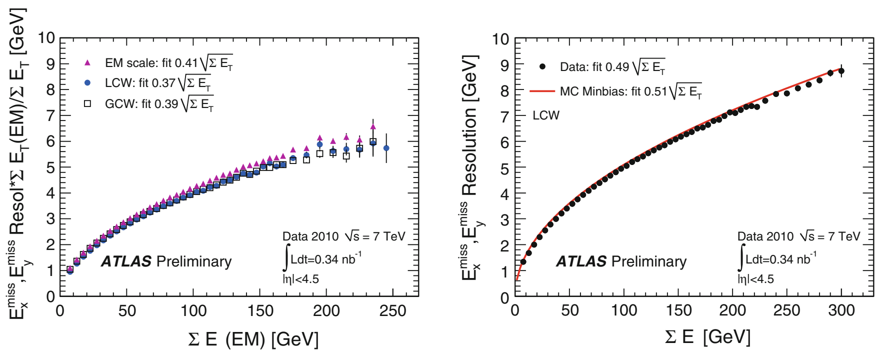

Fig. 2.9 The figure on the *left-hand side* shows the $E_{\mathrm{T}}^{\mathrm{miss}}$ resolution in minimum-bias events for the EM scale $E_{\mathrm{T}}^{\mathrm{miss}}$, and for LCW and GCW calibrated $E_{\mathrm{T}}^{\mathrm{miss}}$. Results are shown as a function of the EM scale ΣE_T. The figure on the *left-hand side* campares the resolution of the LCW $E_{\mathrm{T}}^{\mathrm{miss}}$ in data and MC events. Figures are taken from Ref. [24]

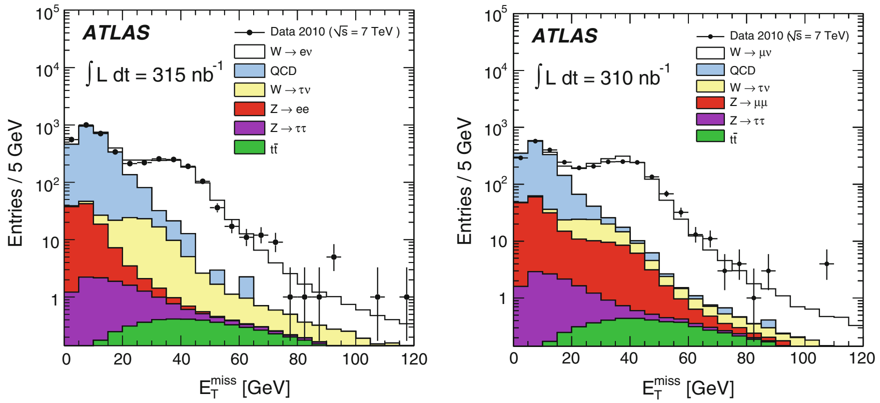

Fig. 2.10 The figure on the *left-hand side* shows $E_{\mathrm{T}}^{\mathrm{miss}}$ distributions in an inclusive sample of events with one electron (*left*) or one muon (*right*) with $p_{\mathrm{T}} > 20\,\mathrm{GeV}$. The figures are taken from Ref. [25]

The LCW $E_{\mathrm{T}}^{\mathrm{miss}}$ calibration scheme has been used successfully in W inclusive and W+jets cross section measurements [25, 26], providing a good understanding of these processes. Figure 2.10 (taken from reference [25]) shows the $E_{\mathrm{T}}^{\mathrm{miss}}$ distributions in an inclusive sample of events with one electron (left) or one muon (right) with $p_{\mathrm{T}} > 20\,\mathrm{GeV}$. The figure shows how the distributions in data and MC are in reasonable agreement, both in the low $E_{\mathrm{T}}^{\mathrm{miss}}$ region ($E_{\mathrm{T}}^{\mathrm{miss}} < 30\,\mathrm{GeV}$) dominated by QCD multi-jet events, and for higher $E_{\mathrm{T}}^{\mathrm{miss}}$ values dominated by W production.

References

1. P. Bryant, L. Evans (eds.), LHC machine. JINST **3**, S08001 (2008)
2. The ALICE Collaboration, The alice experiment at the CERN LHC. JINST **3**, S08002 (2008a)
3. G. Aad et al., The ATLAS experiment at the CERN large hadron collider. JINST **3**, S08003 (2008). doi:10.1088/1748-0221/3/08/S08003
4. The CMS Collaboration, The CMS experiment at the CERN LHC. JINST **3**, S08004 (2008b)
5. The LHCb Collaboration, The LCHb experiment at the CERN LHC. JINST **3**, S08005 (2008c)
6. The ATLAS Collaboration, Studies of the performance of the atlas detector using cosmic-ray muons. Eur. Phys. J. **C 71**, 1593 (2011)
7. The ATLAS Collaboration, Readiness of the ATLAS liquid argon calorimeter for LHC collisions. Eur. Phys. J. **C70**, 723–753 (2010a)
8. The ATLAS Collaboration, Readiness of the ATLAS tile calorimeter for LHC collisions. Eur. Phys. J. **C70**, 11931236 (2010b)
9. G. Aad et al., Luminosity determination in pp collisions at $\sqrt{s} = 7$ TeV using the ATLAS detector at the LHC. Eur. Phys. J. **C71**, 1630 (2011a). doi:10.1140/epjc/s10052-011-1630-5 (24 pages plus author list (36 pages total). 9 Figures, 10 Tables, submitted to Journal EPJC)
10. ATLAS Collaboration, Luminosity determination in pp collisions at $\sqrt{s} = 7$ TeV using the ATLAS detector in 2011 (ATLAS-CONF-2011-116), August 2011a
11. V. Cindro et al., The ATLAS beam conditions monitor. JINST **3**, P02004 (2008b)

12. G. Aad et al., Electron performance measurements with the ATLAS detector using the 2010 LHC proton-proton collision data. Eur. Phys. J. C **72**, 1909 (2012a) (Long author list—awaiting processing)
13. ATLAS Collaboration, Muon performance in minimum bias pp collision data at s = 7 TeV (ATLAS-CONF-2010-036), August 2011b
14. M. Cacciari, G.P. Salam, G. Soyez, The anti-k_t jet clustering algorithm. JHEP **04**, 063 (2008). doi:10.1088/1126-6708/2008/04/063
15. W. Lampl et al., Calorimeter clustering algorithms: description and performance (ATL-LARG-PUB-2008-002), April 2008
16. ATLAS Collaboration, Pile-up corrections for jets from proton-proton collisions at $\sqrt{s} = 7$ TeV in ATLAS in 2011 (ATLAS-CONF-2012-064), July 2012
17. G. Aad et al., Jet energy measurement with the ATLAS detector in proton-proton collisions at $\sqrt{s} = 7$ TeV (2011b)
18. The ATLAS Collaboration, Jet energy scale and its systematic uncertainty for jets produced in proton-proton collisions at $\sqrt{s} = 7$ TeV and measured with the atlas detector (Tech. Rep. ATL-CONF-2010-056), July 2010a
19. The ATLAS Collaboration, In-situ pseudorapidity intercalibration for evaluation of jet energy scale uncertainty using dijet events in proton-proton collisoins at $\sqrt{s} = 7$ TeV (ATL-CONF-2011-014), March 2011c
20. The ATLAS Collaboration, Jet energy resolution and selection efficiency relative to track jets from in-situ techniques with the atlas detector using proton-proton collisions at a center of mass energy $\sqrt{s} = 7$ TeV (Tech. Rep. ATL-CONF-2010-054), July 2010b
21. P. Bagnaia et al., UA2 Collaboration, Measurement of jet production properties at the CERN pp collider. Phys. Lett. B **144**, 283 (1984)
22. B. Abbott et al., D0 Collaboration, High-pT jets in pp collisions at $\sqrt{s} = 630$ GeV and 1800 GeV. Phys. Rev. **D64**, 032003 (2001)
23. T. Barillari et al. http://cdsweb.cern.ch/record/1112035ATL-LARG-PUB-2009-001
24. ATLAS Collaboration, Performance of the missing transverse energy reconstruction and calibration in proton-proton collisions at a center-of-mass energy of $\sqrt{s} = 7$ TeV with the ATLAS detector (ATLAS-CONF-2010-057) (2010c)
25. G. Aad et al., Measurement of the W $\rightarrow$ TeV with the ATLAS detector. JHEP **1012**, 060 (2010). doi:10.1007/JHEP12(2010)060 (38 pages plus author list (57 pages total), 16 figures, 15 tables)
26. The ATLAS Collaboration, Measurement of the production cross section for w-bosons in association with jets in pp collisions at $\sqrt{s} = 7$ TeV with the ATLAS detector. Phys. Lett. **B698**, 325–345 (2011)

Springer

http://www.springer.com/978-3-319-22224-0

Search for Exotic Mono-jet Events
in Proton-Proton Collisions at $\sqrt{s}$=7 TeV and 8 TeV with
the ATLAS Detector
Rossetti, V.
2016, XVII, 164 p., Hardcover
ISBN: 978-3-319-22224-0